RSC Advances

PAPER

View Article Online
View Journal | View Issue

Cite this: *RSC Adv.*, 2017, **7**, 20845

Ultrathin TiO_2 nanosheets synthesized using a high pressure solvothermal method and the enhanced photoresponse performance of $CH_3NH_3PbI_3$–TiO_2 composite films†

Shilong Jiao,‡[a] Xianwei Fu,‡[a] Gang Lian,*[a] Laiying Jing,[a] Zhenghao Xu,[b] Qilong Wang[b] and Deliang Cui*[a]

Received 24th January 2017
Accepted 13th March 2017

DOI: 10.1039/c7ra01073g

rsc.li/rsc-advances

In perovskite–TiO_2 composite optoelectronic devices, a large grain size, a high percentage of {001} facets, TiO_2 nanocrystals with high crystallinity, and good interconnectivity between both TiO_2 and perovskite particles are crucial for the excellent performance of a hybrid photodetector. In this work, a high pressure hydrothermal method was developed to synthesize highly crystalline ultrathin (2–3 nm) TiO_2 nanosheets bound with a high percentage of {001} facets. When these TiO_2 nanosheets were utilized in the fabrication of perovskite–TiO_2 composite photodetectors, a strikingly increased responsivity and detectivity were achieved. Furthermore, when the films were subjected to high pressure thermal treatment, both the particle size and the uniformity of the composite films greatly increased, resulting in a better performance of the hybrid photodetectors.

The power conversion efficiencies (PCEs) of organic–inorganic perovskite solar cells (PSCs) have rapidly reached a remarkable 22.1%,[1] while it was only 3.8% (ref. 2) less than a decade ago. The small effective mass and high mobility of the carriers, a low exciton binding energy and an extremely long exciton diffusion length were found to be responsible for the unprecedented performance of the PSCs.[3–9] Therefore, organic–inorganic perovskites can be widely utilized in the fields of gas sensors,[10] photodetectors[11–15] and lithium ion batteries[16] *etc.* The perovskite $CH_3NH_3PbI_3$ is an ideal active material for photovoltaic devices, as its band gap (~1.5 eV) matches well with the energy of visible and near-IR light. So, the weakly bound excitons with lifetimes as long as ~300 ns are another advantage for their application in photodetectors.[17,18]

TiO_2, one of the most commonly used charge separation layer materials in solar cells, has been investigated intensively using both experimental and theoretical methods, including the tailoring of the facets,[19] impurity doping,[20] surface state simulations,[21,22] photovoltaic and photocatalytic applications,[22–24] and so on. In fact, the {001} facets of anatase TiO_2 are believed to behave better than the {101} facets in both photovoltaic and photocatalytic applications[22,25] because of their higher chemical reactivity. When combined with the perovskite, the bound {001} facets of anatase TiO_2 nanocrystals exhibited much better performance in PSCs[26] and photodetectors.[27] Therefore, the successful synthesis of anatase TiO_2 containing a high percentage of {001} facets (ref. 28) has attracted much attention. Generally, the introduction of F^- is believed to be the most effective strategy to control the growth of the {001} facets of anatase TiO_2 nanocrystals.[29–34] However, excessive F^- can severely etch the {001} facets of TiO_2 nanoflakes and create some defects. Even now, it is still a great challenge to grow ultrathin TiO_2 nanosheets with high crystallinity. It is known that high crystallinity and a low defect density are of great importance in both facilitating the transportation and reducing the recombination centers of photo-generated carriers at the interfaces among different kinds of materials. Therefore, it is essential to develop a modified strategy to grow highly crystalline ultrathin TiO_2 nanosheets with a high percentage of {001} facets combining the effect of F^-.

Our former work has shown that a high pressure can greatly increase the crystallinity and effectively control the growth of the nanocrystals in a solvothermal system.[35] Herein, the ultrathin TiO_2 nanosheets were firstly synthesized using a high pressure solvothermal method. They present high crystallinity and a high percentage of {001} facets. When they were composited with perovskites, the perovskite–TiO_2 nanocomposite films exhibited a strikingly improved responsivity as photodetectors. Furthermore, after the film was treated using a thermal-press method, both the particle size and the

[a]*State Key Lab of Crystal Materials, Shandong University, Jinan 250100, P. R. China. E-mail: liangang@sdu.edu.cn; cuidl@sdu.edu.cn*

[b]*Key Laboratory for Special Functional Aggregated Materials of Education Ministry, School of Chemistry & Chemical Engineering, Shandong University, Jinan 250100, P. R. China*

† Electronic supplementary information (ESI) available. See DOI: 10.1039/c7ra01073g

‡ These authors contributed equally to the work.

uniformity of the film were greatly increased, resulting in the further improvement of their photoresponse performance.

In a typical synthetic process, a certain amount of HF was added to the TBOT (tetrabutyl titanate) solution with stirring for over 30 min. After that, the solution was sealed in a hot-press autoclave (Fig. S1†) and heated to 200 °C at a rate of 5 °C min^{-1}. After the reaction was maintained for 24 h at a pressure of 200 MPa, ultrathin TiO_2 nanosheets formed. The details of the synthetic procedures are described in the ESI† (Experimental section). The product was first analyzed using powder X-ray diffraction (XRD). All of the diffraction peaks (Fig. 1a) match with anatase TiO_2 (JCPDS no. 12-2172) without any crystalline impurities. As depicted in Fig. 1b and S2,† the as-obtained TiO_2 crystals show a uniform rectangular shape and are 50–100 nm in lateral dimension. The high transparency of the TiO_2 nanosheets with respect to the electron beam indicates the ultrathin characteristic of the sample. A typical cross-sectional view shows a thickness of 2–3 nm for the TiO_2 nanosheets (Fig. 1c), which is much thinner than those synthesized using traditional solvothermal methods (Fig. 1d). The suppressed growth of the {001} facets can be deduced from the enhanced adsorption of F^- on the (001) plane at high pressure. Molecular dynamics simulation results indicated that more F^- could be strongly absorbed on the {001} facets at high pressure than at a lower pressure (Fig. 1e), which could obviously suppress the further growth of the nanosheets along the [001] direction at high pressure. Then, ultrathin TiO_2 highly crystalline nanosheets were obtained. The lattice fringes in the magnified HRTEM images are ascribed to the (001) and (101) planes (the inset in Fig. 1c). The top-view HRTEM image of the TiO_2 nanosheets shows the single-crystal character of the nanosheets without any obvious defects. The lattice with a spacing of ~0.35 nm can be indexed to the {101} set of planes (Fig. 1f). To illustrate the effect of F^- on the control of the thickness and defect density, we conducted a series of F^- concentration dependent experiments. It was found that thinner nanosheets were obtained when increasing the F^- concentration from 8 wt% (HF-2) to 15 wt% (HF-4) (Fig. S2–S4†). However, when it was continually increased to 27 wt% (HF-8), the obtained TiO_2 nanosheets were obviously etched and a large amount of dot defects appeared on the {001} facets (Fig. S5†). So, the synergetic effect of F^- and high pressure induces the formation of highly crystalline ultrathin TiO_2 nanosheets.

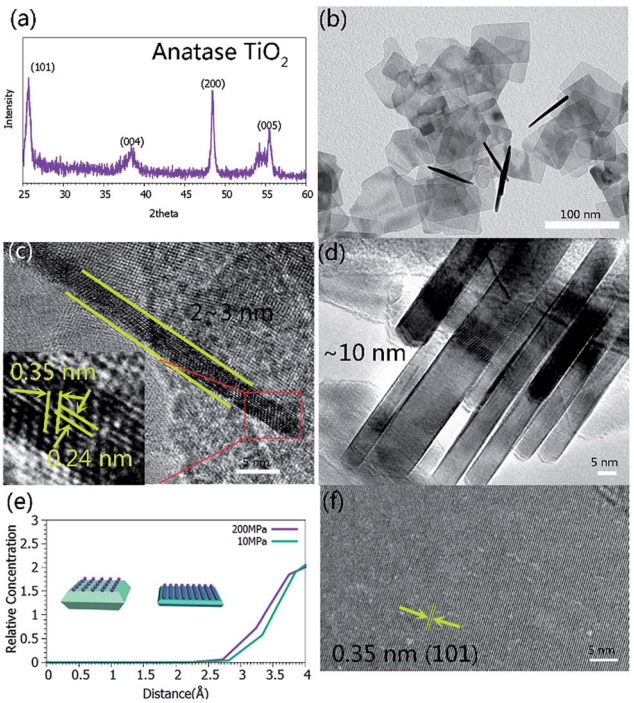

Fig. 1 (a) XRD pattern of the ultrathin anatase TiO_2 nanosheets synthesized *via* a high pressure solvothermal method. (b and c) TEM and side-view HRTEM images of the ultrathin TiO_2 nanosheets. (d) A TEM image of the TiO_2 nanosheets synthesized *via* a conventional solvothermal method. (e) The relative concentration of F^- as a function of the distance from the anatase (001) plane. (f) A top-view HRTEM image of the ultrathin TiO_2 nanosheets.

After the synthesis of highly crystalline and ultrathin anatase TiO_2 nanosheets, they were composited with $CH_3NH_3PbI_3$ to make a photodetector film device. As mentioned above, firstly, high crystallinity and a low defect density of anatase TiO_2 nanosheets can effectively suppress the recombination of the electrons and holes. Secondly, ultrathin TiO_2 nanosheets with a high percentage of {001} facets can more effectively achieve photo-generated carrier transfer on the interfaces.[36–41] Therefore, the synthesized TiO_2 nanosheets are expected to be a promising candidate for enhancing the photoresponse property of $CH_3NH_3PbI_3$ films. In addition, the interface contact of TiO_2 and $CH_3NH_3PbI_3$ also plays a crucial role in improving the behavior of the device.[42–46] It is known that the carriers in the device can easily recombine at the defects and the crystal boundaries that can act as the trapping medium in semiconductors, which is harmful for the device's performance and should be avoided.[47–49] Mohite *et al.* have successfully fabricated perovskite solar cells with millimeter-scale grains that showed a hysteresis-free photovoltaic response.[50] This was attributed to reduced bulk defects and improved charge carrier mobility in the large-grain devices. In addition, Yang *et al.* believed that the carrier recombination in the absorber could be suppressed by carefully controlling the formation of the perovskite layer with large-area grains and low defect density,[51] facilitating carrier injection into the carrier transport layers. So, preparing a detector with a low defect density, few crystal boundaries and large grains will be desirable.

Herein, a novel high pressure thermal treatment method was developed to intensify the interface contact between the TiO_2 nanosheets and the $CH_3NH_3PbI_3$ particles. The details of the procedures are described in the ESI.† As shown in Fig. 2a, the pristine perovskite film mainly consisted of small-sized, non-uniform and irregular particles. The high density grain boundaries, combined with the rough surface of the film, easily resulted in weak photo-generated carrier transfer in the film. When the $CH_3NH_3PbI_3$–TiO_2 films were prepared using a typical spin-coating process, the composite films still presented a similar morphology to the pristine perovskite film (Fig. 2b). In comparison, when the typical film-forming process was followed by a thermal-press treatment, the composite film became

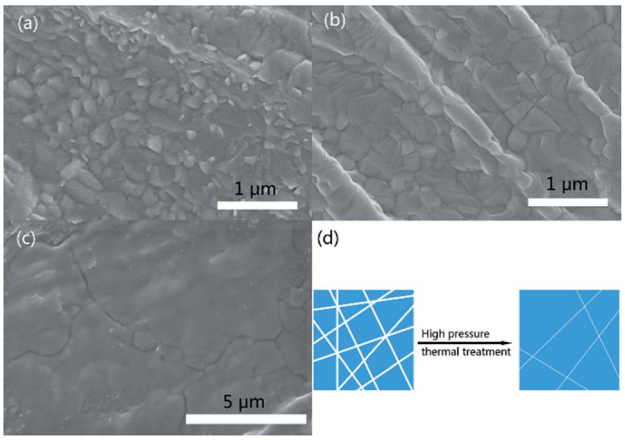

Fig. 2 SEM images of perovskite–TiO_2 composite films. (a) A pure perovskite film. (b) Before and (c) after the high pressure thermal treatment of perovskite-8 wt% TiO_2 (HF-4) films. (d) A schematic illustration of the high pressure thermal treatment on the film.

closely packed and was constructed of much larger grains that were tens of microns in size (Fig. 2c and d), which facilitates the transport of the photo-generated carriers in the composite film. The thickness of the composite film after the high pressure thermal treatment was 1–2 μm (Fig. S6†). Additionally, the high pressure could smooth the film and undoubtedly promote the interfacial contact between $CH_3NH_3PbI_3$ and the TiO_2 nanosheets. Therefore, an enhanced photoresponse performance can be anticipated for the film. To further illustrate the superiority of the highly crystalline ultrathin nanosheets, TiO_2 nanoflakes with different thicknesses and defect densities were also composited with $CH_3NH_3PbI_3$ for comparison.

Because of the excellent optoelectronic characteristics of TiO_2 nanosheets and $CH_3NH_3PbI_3$,[52–56] the composite film was expected to exhibit a strong response towards light illumination. The photoresponse properties of the composite films were investigated in air at room temperature. Fig. 3a presents a schematic diagram of the photodetector fabricated on an Al_2O_3 substrate. The dynamic response curves of the film devices under 532 nm laser irradiation with a power intensity of 20 mW cm^{-2} are presented in Fig. 3b. The responsivity (R), the ratio of the photocurrent to the incident light intensity, indicates how efficiently the detector responds to an optical signal. R is defined as follows:

$$R = \frac{I_{ph}}{P_{light}} \quad (1)$$

where I_{ph} represents the photocurrent in the laser illumination and P_{light} is the incident light intensity. Another important parameter for the photodetector is the detectivity (D^*) which is given by:

$$D^* = \frac{I_{ph}/P_{light}}{(2eI_d)^{1/2}} \quad (2)$$

where e is the elementary charge and I_d is the dark current, which is dominated by the shot noise. Evidently, the dark current should be suppressed as much as possible to distinguish it from weak optical signals. In order to obtain a small value for I_d, a semiconductor film should have a low trap density (demanding the high crystallinity of the components and better boundary contact), low thermal emission rates and good film quality.

In our case, the calculated responsivity is 0.25 mA W^{-1} for the pure perovskite and 1.5 mA W^{-1} for the best performing sample (HF-4) which is about 6 times higher than that of the pure one. The reason for the increase in the responsivity is derived from the well-aligned band structure of the device (Fig. 3c) which allows for rapid charge-carrier separation at the interface, preventing photo-excited electrons in TiO_2 from recombining with holes. Interestingly, the other two samples, namely sample (HF-2) and sample (HF-8), showed a lower responsivity than even the pure perovskite. The reason is still not very clear. The calculated specific detectivity for the sample (HF-4) is 2.5 × 10^{10} Jones (Jones = cm $Hz^{1/2}$ W^{-1}) with an incident laser wavelength of 532 nm. In addition to the above mentioned two important parameters, the linear relationship of the photocurrent with the incident power of the laser is also very crucial to the device's performance. Taking sample (HF-4) as the representative sample, its response to a series of laser power intensities is presented in Fig. 3d and S7,† which clearly indicates a nearly linear relationship between the photocurrent and laser power with the R-square value of 0.98907 (Fig. 3e).

On the other hand, the TiO_2 nanosheets, that were synthesized using a conventional solvothermal method and are denoted as "conventional TiO_2 nanocrystals" (Fig. S4†), were also applied in the fabrication of perovskite–TiO_2 composite film photodetectors (Fig. S8†), in order to compare the photoresponse performances of them with that of the sample (HF-4). The calculated responsivity for the device that was prepared with the conventional TiO_2 nanocrystals is only 0.375 mA W^{-1} (Fig. 4a), which is a little higher than that of the pure perovskite TiO_2 nanocrystals. The photocurrent of the former is almost three times higher than that of the latter. Furthermore, when the sample (HF-4) was treated using a high pressure annealing method, it exhibited a more advanced photo-detecting performance with a calculated responsivity of 2.4 mA W^{-1} (Fig. 4a). The high pressure thermally treated device also showed great linearity between the incident laser power and the photocurrent (Fig. 4b).

As one of the most popular carrier transport materials in perovskite solar cells, anatase TiO_2 nanostructures have been intensively investigated in order to achieve an optimized performance. In order to fully understand the interaction between $CH_3NH_3PbI_3$ and the TiO_2 nanosheets in the composite film, and the response mechanism, we conducted molecular dynamics simulations with an NVT ensemble. A detailed description of the computational process can be found in the ESI.† The radial distribution functions of the two-coordinated oxygen atoms (O_{2c}) in TiO_2 and the hydrogen atoms on the alkyl- (CH–O_{2c}) and amino- (NH–O_{2c}) groups are presented in Fig. 5a. A strong peak at 1.87 Å can be observed for the NH···O_{2c} RDF, while the first peak for the CH···O_{2c} RDF appears at 2.08 Å, indicating that the interaction of NH···O_{2c} is obviously stronger than that of CH···O_{2c}. In comparison, the

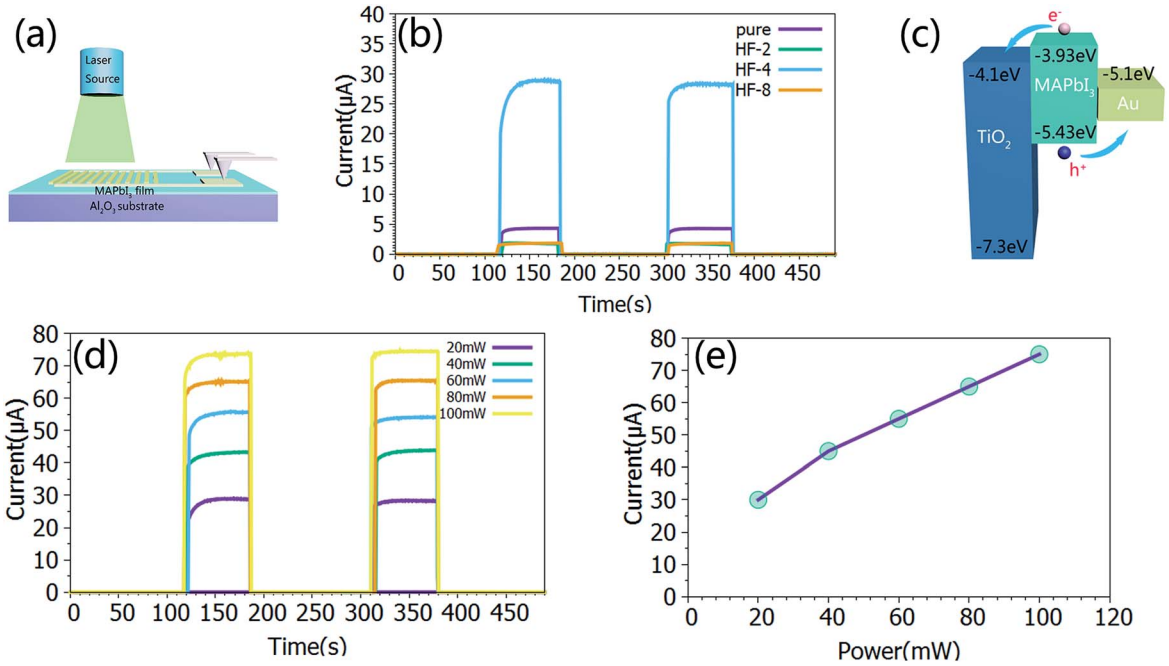

Fig. 3 (a) Schematic illustration of the test device. (b) The dynamic photoresponse of the devices fabricated from pure perovskites and perovskite–TiO_2 composite films. The wavelength and power of the excitation laser are 532 nm and 20 mW, respectively. (c) The band structure of the perovskite and the anatase TiO_2. (d) The dynamic photoresponse of the perovskite-8 wt% TiO_2 (HF-4) film to a 532 nm laser with different power intensities. (e) The corresponding relationship between the laser power and photocurrent for the perovskite-8 wt% TiO_2 (HF-4) film.

RDF of I···O_{2c} exhibits the first strong peak at 3.01 Å (Fig. 5b), which is much larger than that of CH···O_{2c} and NH···O_{2c}, revealing a strikingly weaker interaction between the iodine atom and O_{2c}. Similarly, the interactions between the iodine atom and O_{3c} (a three-coordinated oxygen atom in TiO_2) and Ti_{5c} (a five-coordinated Ti atom in TiO_2) are even weaker. These results reveal that the dominant interfacial interactions in the TiO_2–perovskite composite exist between the hydrogen atom on

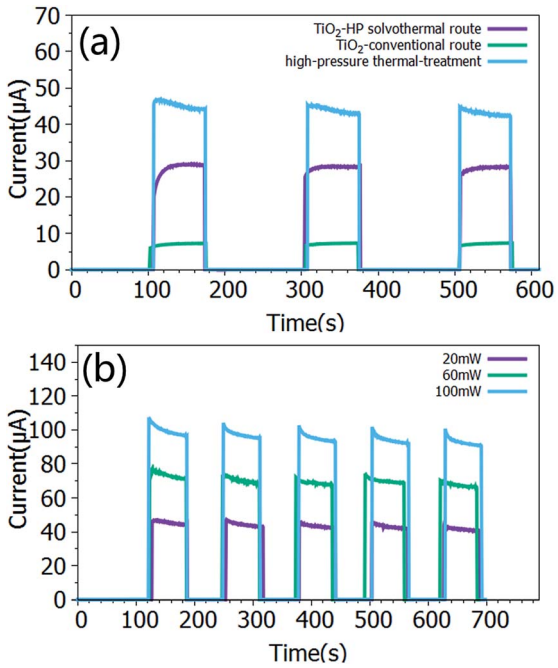

Fig. 4 (a) Comparison of the photoresponse performances of perovskite–TiO_2 composite films fabricated from TiO_2 nanocrystals synthesized using high pressure and conventional solvothermal routes. (b) The dynamic photoresponse of the perovskite-8 wt% TiO_2 (HF-4) film treated using a high pressure annealing process to 532 nm laser light with different power intensities.

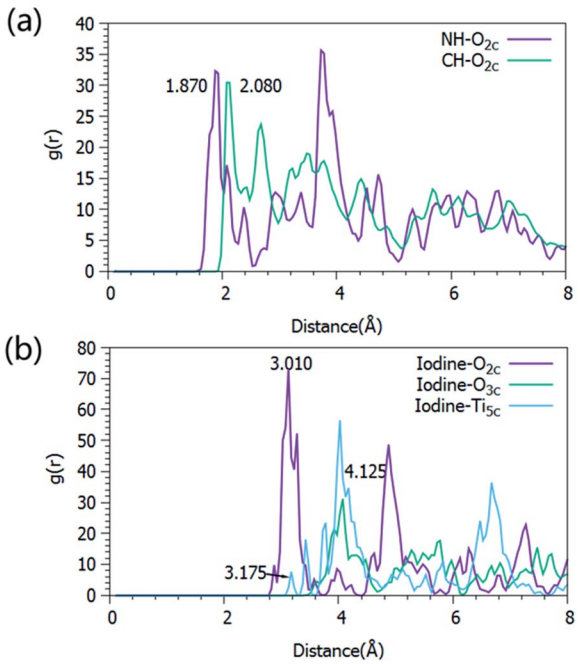

Fig. 5 Radial distribution functions (RDFs) of NH···O_{2c} and CH···O_{2c} (a), and I···O_{2c}, I···O_{3c} and I···Ti_{5c} (b).

the amino-group and the unsaturated oxygen atom in anatase TiO_2. In addition, because there are more unsaturated O_{2c} atoms on the {001} facets of anatase TiO_2, stronger interactions exist between the perovskite and the bound {001} facets of the TiO_2 nanocrystals, which are inevitably more favorable for the transportation of the photo-generated charge carriers between them.

In conclusion, we first developed a high pressure solvothermal method for the synthesis of highly crystalline ultrathin (2–3 nm) TiO_2 nanosheets bound with a high percentage of {001} facets. The high pressure plays a key role in confining the growth of the nanosheets along the [001] direction, combined with the effect of F^-. The $CH_3NH_3PbI_3$–TiO_2 composite films were prepared as hybrid photodetectors. After high pressure thermal treatment of the films, there was obvious growth of the grains, improving their interfacial contact and interconnectivity. As a result, the films presented obviously enhanced responsivity and detectivity, derived from the strikingly improved efficiencies of the photo-generated exciton dissociation and the carrier transportation. Therefore, it is reasonable to believe that the high pressure thermal treatment strategy can be expected to improve the performance of perovskite photovoltaic devices in the future.

Acknowledgements

This work was supported by the Natural Science Foundation of China (NSFC51372143, 51102151, 50990061), Natural Science Foundation of Shandong Province (ZR2011EMQ002, 2013GGX10208) and Independent Innovation Foundation of Shandong University (2012GN051).

Notes and references

1 M. Saliba, T. Matsui, K. Domanski, J.-Y. Seo, A. Ummadisingu, S. M. Zakeeruddin, J.-P. Correa-Baena, W. R. Tress, A. Abate, A. Hagfeldt and M. Grätzel, *Science*, 2016, **354**, 206–209.
2 A. Kojima, K. Teshima, Y. Shirai and T. Miyasaka, *J. Am. Chem. Soc.*, 2009, **131**, 6050–6051.
3 M. B. Johnston and L. M. Herz, *Acc. Chem. Res.*, 2016, **49**, 146–154.
4 G. E. Eperon, S. D. Stranks, C. Menelaou, M. B. Johnston, L. M. Herz and H. J. Snaith, *Energy Environ. Sci.*, 2014, **7**, 982–988.
5 S. Luo and W. A. Daoud, *J. Mater. Chem. A*, 2015, **3**, 8992–9010.
6 Q. Lin, A. Armin, R. Chandra, R. R. C. R. Nagiri, P. L. Burn, P. Meredith, G. E. Eperon, S. D. Stranks, C. Menelaou, M. B. Johnston, L. M. Herz, H. J. Snaith, N. J. Jeon, J. H. Noh, Y. C. Kim, W. S. Yang, S. Ryu and S. Il Seok, *Nat. Mater.*, 2014, **13**, 1–7.
7 Q. Lin, A. Armin, R. Chandra, R. R. C. R. Nagiri, P. L. Burn and P. Meredith, *Nat. Photonics*, 2014, **9**, 106–112.
8 D. Shi, V. Adinolfi, R. Comin, M. Yuan, E. Alarousu, A. Buin, Y. Chen, S. Hoogland, A. Rothenberger, K. Katsiev, Y. Losovyj, X. Zhang, P. A. Dowben, O. F. Mohammed, E. H. Sargent and O. M. Bakr, *Science*, 2015, **347**, 519–522.
9 S. D. Stranks, S. D. Stranks, G. E. Eperon, G. Grancini, C. Menelaou, M. J. P. Alcocer, T. Leijtens, L. M. Herz, A. Petrozza and H. J. Snaith, *Science*, 2014, **342**, 341–344.
10 Y. Liu, Y. Luo, A. A. Elzatahry, W. Luo, R. Che, J. Fan, K. Lan, A. M. Al-enizi, Z. Sun, B. Li, Z. Liu, D. Shen, Y. Ling and C. Wang, *ACS Cent. Sci.*, 2015, **1**, 400–440.
11 H. R. Xia, J. Li, W. T. Sun and L. M. Peng, *Chem. Commun.*, 2014, **50**, 13695–13697.
12 X. Hu, X. Zhang, L. Liang, J. Bao, S. Li, W. Yang and Y. Xie, *Adv. Funct. Mater.*, 2014, **24**, 7373–7380.
13 X. Hu, K. Wang, C. Liu, T. Meng, Y. Dong, S. Liu, F. Huang, X. Gong and Y. Cao, *J. Mater. Chem. C*, 2014, **2**, 9592–9598.
14 Y. Zhang, J. Du, X. Wu, G. Zhang, Y. Chu, D. Liu, Y. Zhao, Z. Liang and J. Huang, *ACS Appl. Mater. Interfaces*, 2015, 21634–21638.
15 C. Bao, W. Zhu, J. Yang, F. Li, S. Gu, Y. Wang, T. Yu, J. Zhu, Y. Zhou and Z. Zou, *ACS Appl. Mater. Interfaces*, 2016, **8**, 23868–23875.
16 H.-R. Xia, W. Sun and L.-M. Peng, *Chem. Commun.*, 2015, **51**, 13787–13790.
17 A. Marchioro, J. Teuscher, D. Friedrich, M. Kunst, R. van de Krol, T. Moehl, M. Gratzel and J.-E. Moser, *Nat. Photonics*, 2014, **8**, 250–255.
18 C. Wehrenfennig, G. E. Eperon, M. B. Johnston, H. J. Snaith and L. M. Herz, *Adv. Mater.*, 2014, **26**, 1584–1589.
19 G. Liu, H. G. Yang, J. Pan, Y. Q. Yang, G. Q. M. Lu and H. M. Cheng, *Chem. Rev.*, 2014, **114**, 9559–9612.
20 Y. Bai, F. D. Angelis, J. Bisquert and P. Wang, *Chem. Rev.*, 2014, **114**, 10131–10176.
21 R. Asahi, T. Morikawa, H. Irie and T. Ohwaki, *Chem. Rev.*, 2014, **114**, 9824–9852.
22 F. De Angelis, C. Di Valentin, S. Fantacci, A. Vittadini and A. Selloni, *Chem. Rev.*, 2014, **114**, 9708–9753.
23 K. Bourikas, C. Kordulis and A. Lycourghiotis, *Chem. Rev.*, 2014, **114**, 9754–9823.
24 Y. Ma, X. L. Wang, Y. S. Jia, X. B. Chen, H. X. Han and C. Li, *Chem. Rev.*, 2014, **114**, 9987–10043.
25 Y. Bai, I. Mora-Seró, F. De Angelis, J. Bisquert and P. Wang, *Chem. Rev.*, 2014, **114**, 10095–10130.
26 M. I. Dar, F. J. Ramos, Z. Xue, B. Liu, S. Ahmad, S. A. Shivashankar, M. K. Nazeeruddin and M. Gratzel, *Chem. Mater.*, 2014, **26**, 4675–4678.
27 H. R. Xia, J. Li, W. T. Sun and L. M. Peng, *Chem. Commun.*, 2014, **50**, 13695–13697.
28 H. G. Yang, C. H. Sun, S. Z. Qiao, J. Zou, G. Liu, S. C. Smith, H. M. Cheng and G. Q. Lu, *Nature*, 2008, **453**, 638–641.
29 X. Zhao, W. Jin, J. Cai, J. Ye, Z. Li, Y. Ma, J. Xie and L. Qi, *Adv. Funct. Mater.*, 2011, **21**, 3554–3563.
30 J. S. Chen, C. Chen, J. Liu, R. Xu, S. Z. Qiao and X. W. Lou, *Chem. Commun.*, 2011, **47**, 2631–2633.
31 J. Yu, J. Low, W. Xiao, P. Zhou and M. Jaroniec, *J. Am. Chem. Soc.*, 2014, **136**, 8839–8842.
32 J. Y. Zheng, S. H. Bao, Y. Guo and P. Jin, *ACS Appl. Mater. Interfaces*, 2014, **6**, 5940–5946.

33 Z. Wang, K. Lv, G. Wang, K. Deng and D. Tang, *Appl. Catal., B*, 2010, **100**(1–2), 378–385.
34 K. Lv, B. Cheng, J. Yu and G. Liu, *Phys. Chem. Chem. Phys.*, 2012, **14**(16), 5349.
35 J. Wang, G. Lian, H. Si, Q. Wang, D. Cui and C. P. Wong, *ACS Nano*, 2016, **10**, 405–412.
36 T. Tachikawa, S. Yamashita and T. Majima, *J. Am. Chem. Soc.*, 2011, **133**, 7197–7204.
37 X. H. Yang, Z. Li, G. Liu, J. Xing, C. Sun, H. G. Yang and C. Li, *CrystEngComm*, 2011, **13**, 1378.
38 J. Yu, J. Low, W. Xiao, P. Zhou and M. Jaroniec, *J. Am. Chem. Soc.*, 2014, **136**, 8839–8842.
39 N. Roy, Y. Sohn and D. Pradhan, *ACS Nano*, 2013, **7**, 2532–2540.
40 X. H. Yang, Z. Li, C. Sun, H. G. Yang and C. Li, *Chem. Mater.*, 2011, **23**, 3486–3494.
41 J. Yu, J. Fan and K. Lv, *Nanoscale*, 2010, **2**, 2144–2149.
42 J. Min, Z. Zhang, Y. Hou, C. O. Ramírez Quiroz, T. Przybilla, C. Bronnbauer, F. Guo, K. Forberich, H. Azimi, T. Ameri, E. Spiecker, Y. Li and C. J. Brabec, *Chem. Mater.*, 2015, **27**(1), 227–234.
43 B. Bouthinon, R. Clerc, J. Vaillant, J. M. Verilhac, J. Faure-Vincent, D. Djurado, I. Ionica, G. Man, A. Gras, G. Pananakakis, R. Gwoziecki and A. Kahn, *Adv. Funct. Mater.*, 2015, **25**(7), 1090–1101.
44 J. Qi, X. Zhou, D. Yang, W. Qiao, D. Ma and Z. Y. Wang, *Adv. Funct. Mater.*, 2014, **24**(48), 7605–7612.
45 Y. S. Lee, J. Heo, S. C. Siah, J. P. Mailoa, R. E. Brandt, S. B. Kim, R. G. Gordon and T. Buonassisi, *Energy Environ. Sci.*, 2013, **6**(7), 2112–2118.
46 Y. S. Lee, J. Heo, S. C. Siah, J. P. Mailoa, R. E. Brandt, S. B. Kim, R. G. Gordon and T. Buonassisi, *Energy Environ. Sci.*, 2013, **6**(7), 2112–2118.
47 F. Hao, C. C. Stoumpos, Z. Liu, R. P. H. Chang and M. G. Kanatzidis, *J. Am. Chem. Soc.*, 2014, **136**, 16411–16419.
48 Y. Li, Y. Zhao, Q. Chen, Y. Yang, Y. Liu, Z. Hong, Z. Liu, Y. T. Hsieh, L. Meng, Y. Li and Y. Yang, *J. Am. Chem. Soc.*, 2015, **137**, 15540–15547.
49 L. F. Yang, X. G. Yu, M. S. Xu, H. Z. Chen and D. R. Yang, *J. Mater. Chem. A*, 2014, **2**, 16877–16883.
50 W. Nie, H. Tsai, R. Asadpour, J.-C. Blancon, A. J. Neukirch, G. Gupta, J. J. Crochet, M. Chhowalla, S. Tretiak, M. A. Alam, H.-L. Wang and A. D. Mohite, *Science*, 2015, **347**(6221), 522–525.
51 H. Zhou, Q. Chen, G. Li, S. Luo, T. Song, H.-S. Duan, Z. Hong, J. You, Y. Liu and Y. Yang, *Science*, 2014, **345**(6196), 542–547.
52 W. Chen, Y. Wu, Y. Yue, J. Liu, W. Zhang, X. Yang, H. Chen, E. Bi, I. Ashraful, M. Grätzel and L. Han, *Science*, 2015, **350**, 944–948.
53 H. S. Jung and N.-G. Park, *Small*, 2014, 1–16.
54 M. I. Saidaminov, M. A. Haque, M. Savoie, A. L. Abdelhady, N. Cho, I. Dursun, U. Buttner, E. Alarousu, T. Wu and O. M. Bakr, *Adv. Mater.*, 2016, 1–6.
55 H.-S. Kim, J.-W. Lee, N. Yantara, P. P. Boix, S. A. Kulkarni, S. Mhaisalkar, M. Grätzel and N.-G. Park, *Nano Lett.*, 2013, **13**, 2412–2417.
56 O. Malinkiewicz, A. Yella, Y. H. Lee, G. M. M. Espallargas, M. Graetzel, M. K. Nazeeruddin and H. J. Bolink, *Nat. Photonics*, 2014, **8**, 128–132.